ARTICLE

Check for updates

Carboxyl-richness controls organic carbon preservation during coprecipitation with iron (oxyhydr)oxides in the natural environment

Lisa Curti [1], Oliver W. Moore [1], Peyman Babakhani[1], Ke-Qing Xiao [1], Clare Woulds[1], Andrew W. Bray[1], Ben J. Fisher [1], Majid Kazemian [2], Burkhard Kaulich[2] & Caroline L. Peacock [1]✉

The coprecipitation of organic carbon with iron minerals is important for its preservation in soils and sediments, but the mechanisms for carbon-iron interactions and thus the controls on organic carbon cycling are far from understood. Here we coprecipitate carboxylic acids with iron (oxyhydr)oxide ferrihydrite and use near-edge X-ray absorption fine structure spectroscopy and wet chemical treatments to determine the relationship between sequestration mechanism and organic carbon stability against its release and chemical oxidative remineralisation. We show that organic carbon sequestration, stabilisation and persistence increase with an increasing number of carboxyl functional groups. We suggest that carboxyl-richness provides an important control on organic carbon preservation in the natural environment. Our work offers a mechanistic basis for understanding the stability and persistence of organic carbon in soils and sediments, which might be used to develop an overarching relationship between organic functional group-richness, mineral interactions and organic carbon preservation in the Earth system.

[1] School of Earth and Environment, University of Leeds, Leeds LS2 9JT, UK. [2] Diamond Light Source Ltd., Harwell Science and Innovation Campus, Didcot, Oxfordshire OX11 0DE, UK. ✉email: C.L.Peacock@leeds.ac.uk

The sequestration of organic carbon (OC) by iron (oxyhydr) oxides in soils and sediments provides a 'rusty sink' for OC[1,2] that helps generate and maintain soil function[3,4], mitigate against climate change[5,6] and enhance the burial of OC for regulation of atmospheric CO_2 and O_2 over geological time[2]. Despite the importance of OC–iron (oxyhydr)oxide phases, however, the mechanisms responsible for OC sequestration, stabilisation against remineralisation and persistence with iron (oxyhydr)oxides are poorly understood[1]. At first glance, most OC and iron (oxyhydr)oxides are transient, with OC subject to extensive remineralisation[7] and reactive iron (oxyhydr)oxides reductively dissolved or transformed into more crystalline forms during diagenesis[8]. The sequestration of OC by iron (oxyhydr) oxides, however, results in the persistence of OC–iron phases in both oxic and anoxic soils and sediments over hundreds to thousands of years[2,9].

The sequestration of OC with iron (oxyhydr)oxides typically occurs through a variety of sequestration processes that remove OC from solution to the solid mineral particles[10]. Sequestration processes can include the surface sorption, or adsorption, of OC to preformed mineral particles and the coprecipitation of OC with neoformed mineral phases, where OC is removed from solution as a consequence of mineral precipitation[11–13]. During coprecipitation, OC can become adsorbed at particle surfaces and incorporated into particle interiors[11]. In soils and sediments, OC is often present in the porewaters from which iron (oxyhydr) oxides precipitate, and thus the coprecipitation of OC with these minerals is a common process for OC–iron (oxyhydr)oxide formation[11–14] that is recently shown to be quantitatively important for OC persistence on a global scale[2,15].

Despite the importance of the sequestration of OC with iron (oxyhydr)oxides via coprecipitation, relatively little is known about coprecipitation sequestration mechanisms or how these stabilise OC against remineralisation. Coprecipitation with OC can stabilise iron (oxyhydr)oxides because the association of OC with the mineral particles can kinetically retard reductive dissolution[16–19] and mineral transformation[18,20,21]. Coprecipitated OC in turn might be stabilised by an adsorption and/or incorporation mechanism that limits exposure of the sequestered OC to remineralisation[15]. Such an adsorption mechanism would need to rapidly remove OC from the remineralisable dissolved pool and strongly bind it to mineral particles, so that it undergoes only limited desorption back into the dissolved reservoir[22]. Similarly, an incorporation mechanism must locate OC inside mineral pore spaces for example, where it can become adsorbed and/or is otherwise physically inaccessible to remineralisation[23].

Previous experimental work on the sequestration of OC during coprecipitation with iron (oxyhydr)oxides indicates that the adsorption of carboxyl functional groups to mineral particles is a dominant coprecipitation sequestration mechanism, involving the formation of outer-sphere[12] or inner-sphere complexes, the latter involving carboxyl ligand exchange between an OH of a carboxyl group and an OH of a mineral site[14]. Previous experimental work on the sequestration of OC during adsorption with preformed iron (oxyhydr)oxides also indicates that carboxyl ligand exchange might result in strongly adsorbed OC[9,24–26] with increased resistance to remineralisation[27]. All these studies, however, use natural organic matter (NOM), which is an extremely complex mixture containing a variety of different organic functional groups[28]. This complexity together with differences between types of NOM in terms of sources, ages and diagenetic histories has therefore precluded a systematic investigation of the relationship between a carboxyl sequestration mechanism and OC stabilisation against remineralisation[29]. Indeed a link between particular binding mechanisms and OC persistence is only presumed and has never been systematically investigated[30].

Here we take a direct mechanistic approach to determine how carboxyl-rich OC is sequestered during coprecipitation with iron (oxyhydr)oxides, and how this sequestration mechanism controls the stabilisation of OC against its release and chemical oxidative remineralisation. We perform controlled coprecipitation experiments, using a series of simple carboxylic acids as model organic compounds and the iron (oxyhydr)oxide ferrihydrite. We use scanning transmission X-ray microscopy and near-edge X-ray absorption fine structure spectroscopy (STXM NEXAFS) to determine OC sequestration mechanism, and a variety of wet chemical treatments to determine the relationship between OC sequestration mechanism and stabilisation against its release and oxidation. Finally, we apply a kinetic model to our wet chemical data to quantify OC persistence over time. Our work shows that simple carboxylic acids are sequestered during coprecipitation with ferrihydrite via a carboxyl ligand exchange adsorption mechanism occurring predominantly at the ferrihydrite surface. We show that an increasing number of carboxyl groups directly increases OC sequestration via multi-carboxyl ligand exchange. We demonstrate that this multi-carboxyl adsorption mechanism increases the stability of OC against desorption and oxidation and results in a pool of non-desorbable OC that might persist with iron (oxyhydr)oxides in soils and sediments. Our work indicates that OC persistence at least partly depends on its carboxyl-richness and the association of this OC fraction with iron (oxyhydr)oxides. Our results also indicate that using the amount of OC and reactive iron to predict OC sequestration is insufficient and rather our work provides a mechanistic platform from which organic functional group-richness might be used as a basis for predicting the stability and persistence of OC in the natural environment.

Results

Establishing a model system for carboxyl–iron (oxyhydr)oxide coprecipitation. To represent carboxyl-rich OC, we chose a selection of saturated aliphatic mono-, di- and tri-carboxylic acids containing only COOH carboxyl and CH methyl groups (Fig. 1). These acids are directly relevant to soil and sediment porewaters where they and other low molecular weight organic acids are prevalent[31,32]. They also serve as model organic compounds for understanding the role of carboxyl groups in the sequestration of more complex dissolved NOM[33], which is recently shown to comprise a number of universal molecular structures containing predominantly carboxyl and hydroxyl groups[34]. To represent iron (oxyhydr)oxides, we chose ferrihydrite, which is abundant and commonly associated with OC in the natural environment[8].

We investigate sequestration, stabilisation and persistence of the acids with respect to the number of carboxyl groups (n) at constant number of total carbon atoms (m) and the number of total carbon atoms (m) at constant number of carboxyl groups (n) (Fig. 1, comparing across (sequentially increasing n) or down columns (sequentially increasing m)). The corresponding coprecipitates are denoted Fh_acid$n$/m_C:Fe, where Fh is ferrihydrite, acid indicates the first three letters of the systematic IUPAC name followed by n carboxyl groups and m total carbon atoms and C:Fe is the molar C:Fe ratio of the solid phase. In the following sections, the results are described for the entire data set and then for specific data subsets with either increasing n/constant m or constant n/increasing m. Data subset Fh_Pen1/5 – Fh_Pen2/5 – Fh_Eth3/5 (green, blue and purple solid squares, respectively, Fig. 1) is described for all results.

Increasing number of carboxyl groups promotes carbon sequestration. To investigate the sequestration of the acids with ferrihydrite, each acid was coprecipitated with ferrihydrite at a
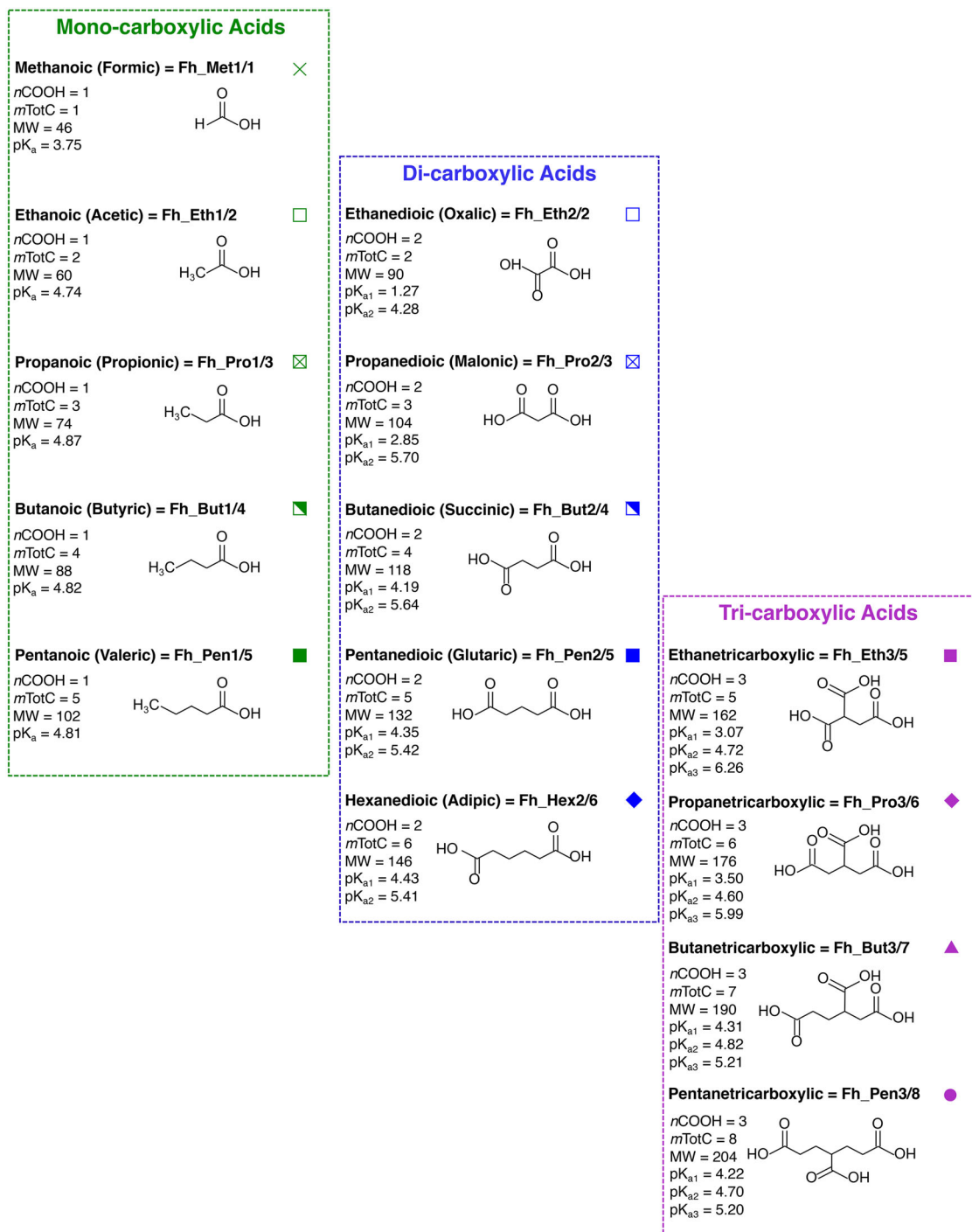
Fig. 1 Schematic showing mono-, di- and tri-carboxylic acids coprecipitated with iron (oxyhydr)oxide ferrihydrite. Mono-, di- and tri-carboxylic acids, including systematic IUPAC name, common name for reference in parentheses, coprecipitate nomenclature and coprecipitate data symbol; number of carboxyl functional groups (nCOOH); number of total carbon atoms (mTotC); molecular weight (MW); and pK_a of the carboxyl functional groups (available at Pubchem[85] or calculated using the ACD/Labs I-Lab 2.0 software (algorithm version: v12.1.0.50374)). For the coprecipitate nomenclature, coprecipitates are denoted Fh_acidn/m, where Fh is ferrihydrite, acid indicates the first three letters of the systematic IUPAC name followed by n carboxyl groups and m total carbon atoms. Individual coprecipitates are denoted Fh_acidn/m_C:Fe where C:Fe is the molar C:Fe ratio of the solid phase. For the coprecipitate data symbol, coprecipitates are represented by a consistent data symbol, where colour indicates the number of carboxyl groups n (green, blue and purple $= n$ 1, 2, 3 carboxyl groups, respectively), and shape indicates the number of total carbon atoms m (crosses, open squares, crossed open squares, half solid squares, solid squares, solid diamonds, solid triangles, solid circles $= m$ 1, 2, 3, 4, 5, 6, 7, 8 total carbon atoms, respectively). Influence of the number of carboxyl groups n at constant number of total carbon atoms m on OC sequestration, stabilisation and persistence is investigated by comparing acids across the columns (sequentially increasing n). Influence of the number of total carbon atoms m at constant number of carboxyl groups n on OC sequestration, stabilisation and persistence is investigated by comparing acids down the columns (sequentially increasing m).
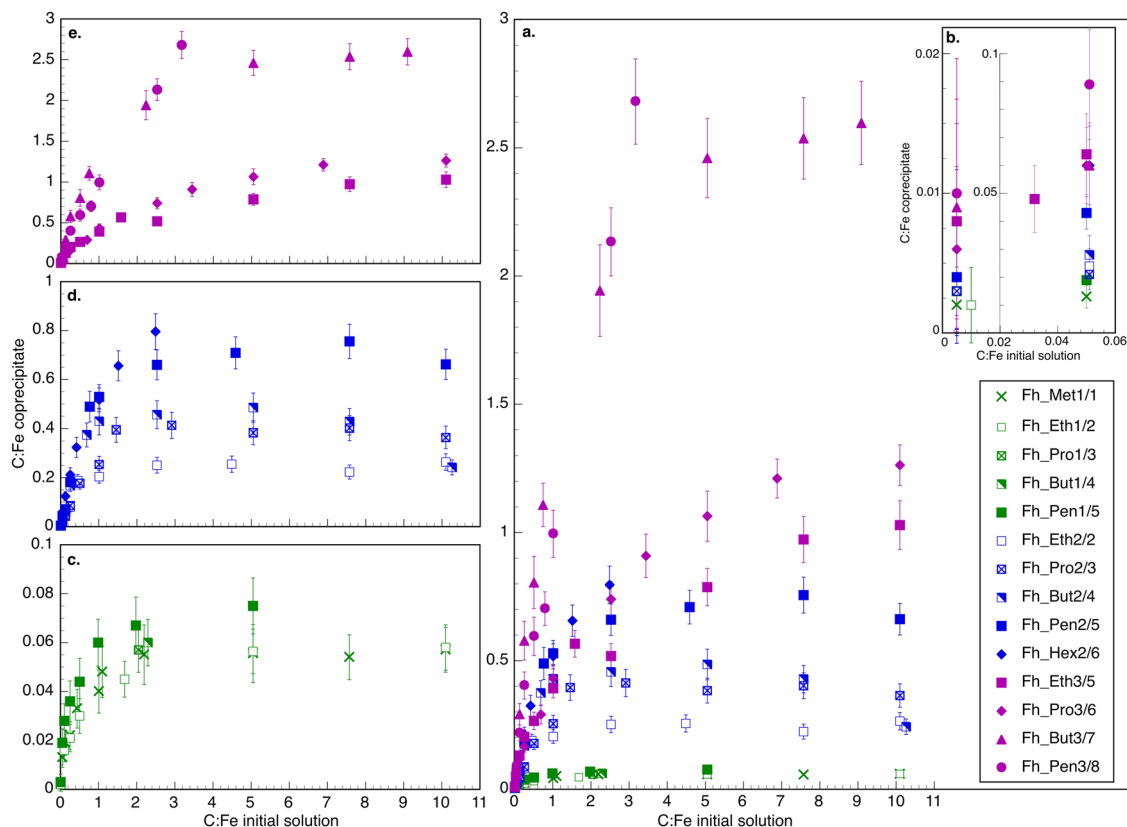
Fig. 2 Sequestration of mono-, di- and tri-carboxylic acids during coprecipitation with iron (oxyhydr)oxide ferrihydrite. Sequestration data for carboxylic acid ferrihydrite coprecipitates plotted as C:Fe molar ratio of initial coprecipitation solution vs. C:Fe molar ratio of resulting coprecipitate: **a** mono-, di- and tri-carboxylic coprecipitates for comparison, and **b** inset of mono-, di- and tri-carboxylic coprecipitates at low C:Fe initial solution; **c** mono-carboxylic coprecipitates; **d** di-carboxylic coprecipitates; **e** tri-carboxylic coprecipitates. Green, blue and purple colour codes depict mono-, di- and tri-carboxylic data, respectively. The coprecipitate nomenclature is given in Fig. 1. Symbols are as follows: cross: Fh_Met1/1; open square: Fh_Eth1/2 and Fh_Eth2/2; crossed open square: Fh_Pro1/3 and Fh_Pro2/3; half solid square: Fh_But1/4 and Fh_But2/4; solid square: Fh_Pen1/5, Fh_Pen2/5 and Fh_Eth3/5; solid diamond: Fh_Hex2/6 and Fh_Pro3/6; solid triangle: Fh_But3/7; solid circle: Fh_Pen3/8. Data points and error bars represent the mean and one standard error of the mean (1 SEM) for triplicate coprecipitates each measured in triplicate. Errors are propagated through all calculations using standard error propagation rules.
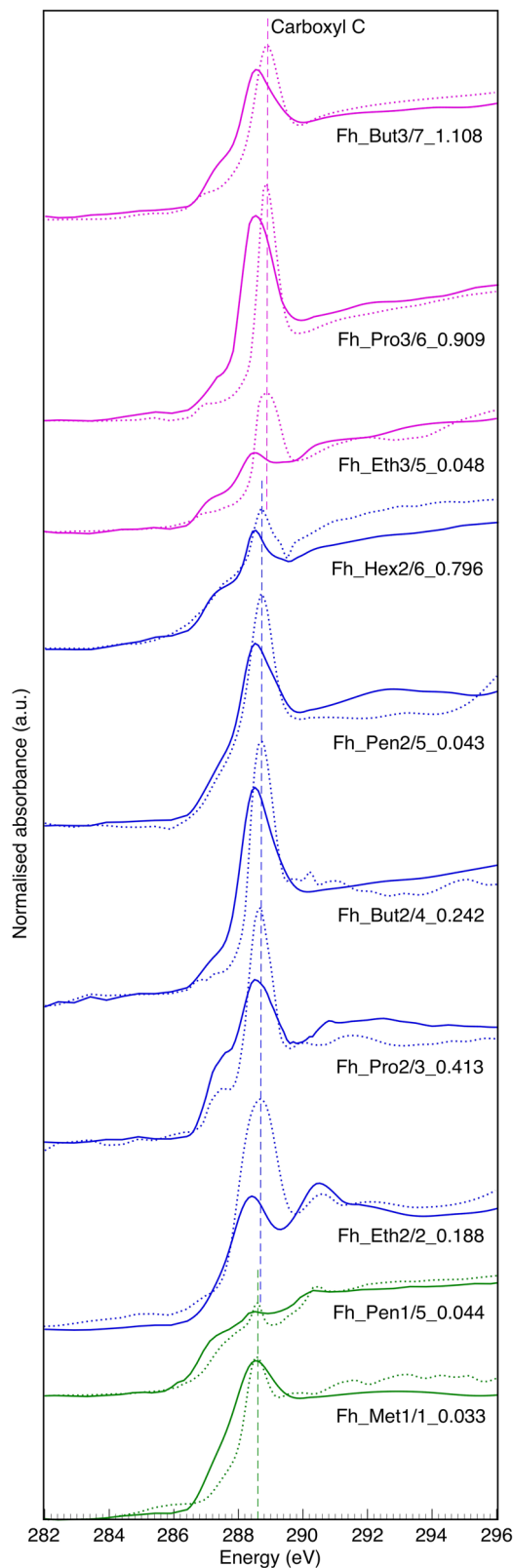
sequentially increasing initial carbon and fixed initial iron concentration (see 'Methods').

The entire data set shows that, as the number of carboxyl groups increases, the molar amount of OC sequestered increases ($R^2 = 0.728$, Supplementary Fig. 1) from a maximum of 0.87 mmol C g^{-1} (0.075 C:Fe) for the mono-carboxyl coprecipitates to 15 mmol C g^{-1} (2.681 C:Fe) for the tri-carboxyl coprecipitates (Fig. 2a). Additionally as the number of total carbon atoms increases, the molar amount of OC sequestered increases ($R^2 = 0.733$, Supplementary Fig. 2) and thus the maximum ranges between 0.67–0.87, 2.7–7.9 and 6.7–15 mmol C g^{-1} (0.056–0.075, 0.264–0.796 and 1.029–2.681 C:Fe) for the mono-, di- and tri-carboxyl coprecipitates, respectively (Fig. 2c–e). All data subsets corroborate the above trends, with the molar amount of OC sequestered generally increasing for all those with increasing n/constant m (e.g. Fh_Pen1/5_0.019 – Fh_Pen2/5_0.043 – Fh_Eth3/5_0.064 at initial solution C:Fe ≈ 0.05, $R^2 = 0.996$, Supplementary Fig. 1), and constant n/increasing m (e.g. Fh_Met1/1_0.013 up to Fh_Pen1/5_0.019 at initial solution C:Fe ≈ 0.05, $R^2 = 0.923$, Supplementary Fig. 2) (Supplementary Data 1). Thus, with increasing number of carboxyl groups and number of total carbon atoms, the acids have increasing affinity for ferrihydrite.

The consistent increase in the sequestration maximum as a function of the number of carboxyl groups and the total number of carbon atoms suggests that total sequestration is not controlled

by the capacity of ferrihydrite to sequester OC but rather by the affinity of OC for ferrihydrite[35]. The capacity of the particles to sequester OC is difficult to evaluate, however, because it is a function of both the adsorption capacity and the amount of OC that can be incorporated into the particle interiors. The adsorption capacity can be equated to the surface coverage, but this can be variably defined because adsorbed OC can exist in both monolayer (or monolayer equivalent[36]) and multilayer coatings[37–39]. The incorporation capacity is similarly complicated because there likely exists a continuum between OC–iron macromolecules and OC–iron (oxyhydr)oxide particles that have highly elevated C:Fe[2,14,15].

If we define the theoretical adsorption capacity as the surface coverage of a monolayer, however, and we nominally assume that all our OC is adsorbed in a monolayer, then we can compare our theoretical and measured surface coverages to hypothetically determine whether our sequestered OC could be entirely accommodated in a monolayer or whether multilayers and/or incorporation into particle interiors is additionally required to achieve our OC loadings. We consider adsorption scenarios in which either just one COOH group from each acid molecule binds to a FeOH adsorption site (one-carboxyl adsorption) or all COOH groups from each acid molecule each bind to a FeOH adsorption site (two-carboxyl and three-carboxyl adsorption for di- and tri-carboxylic acids, respectively) (see 'Methods',

Fig. 3 Carbon 1s NEXAFS spectra for mono-, di- and tri-carboxylic acids coprecipitated with iron (oxyhydr)oxide ferrihydrite. Carbon 1s NEXAFS spectra for carboxylic acid standards (dotted lines) and carboxylic acid ferrihydrite coprecipitate samples (solid lines) plotted as energy (eV) vs. normalised absorbance (arbitrary units). Green, blue and purple colour codes depict mono-, di- and tri-carboxylic data, respectively. The coprecipitate nomenclature is given in Fig. 1. Spectra are stacked with an arbitrary offset for clarity. Carboxyl carbon peak positions for the unreacted mono-, di- and tri-carboxylic acid standards are shown with vertical dashed green, blue and purple lines, respectively, and appear at slightly higher energy as the number of carboxyl groups increases. Carboxyl carbon peak positions for the coprecipitate samples are shifted to lower energy compared to their respective standards, and this shift becomes increasingly pronounced with increasing number of carboxyl groups.

some of the tri-carboxyl coprecipitates with the highest sequestrations, however, provide ~17% less sequestration capacity assuming the one- and two-carboxyl scenarios (last data point for Fh_Pen3/8, with C:Fe 2.681, Fig. 2) and ~7–76% less sequestration capacity assuming the three-carboxyl scenario (last 2–3 data points for each tri-carboxyl coprecipitate, with C:Fe 0.787–2.681, Fig. 2), than would be required for only monolayer adsorption (Supplementary Data 2). Thus, almost all our acids could theoretically be adsorbed in a monolayer at the particle surfaces, without requiring any extra sequestration capacity that might be provided by adsorption in multilayers and/or incorporation into particle interiors[11,40]. The tri-carboxylic acids with the highest sequestrations, however, are likely also adsorbed in multilayers[37–39] and/or are incorporated into OC–iron macro-molecules or particle interiors[2,15,23,41].

Increasing number of carboxyl groups promotes multi-carboxyl carbon sequestration. To determine the sequestration mechanisms of the acids with ferrihydrite, we subject our coprecipitates to STXM NEXAFS (see 'Methods'). We chose coprecipitates (Supplementary Data 1) encompassing a range of molar OC (but excluding the tri-carboxylic coprecipitates with the highest sequestrations) and including several data subsets with approximately constant molar OC and either increasing n/ constant m or constant n/increasing m (see 'Methods').

The NEXAFS spectra exhibit one major peak at ~288.6 eV (Fig. 3 and Supplementary Data 3) corresponding to carboxyl carbon ($\pi^*_{C=O}$, 287.7–289 eV; Supplementary Table 1). The exact carboxyl peak position of all the unreacted mono-, di- and tri-carboxylic acid standards occurs at 288.6 ± 0.05, 288.7 ± 0.05 and 288.9 ± 0.05 eV, respectively, and thus appears at slightly higher energy as the number of carboxyl groups increases (Supplementary Table 2). Migration of the carbon 1s-π^* transition occurs because the carbon 1s electron is bound more tightly as more electron-withdrawing atoms (such as oxygen in our acids) are added to an organic structure[42]. Compared to their respective standards, the carboxyl peak for all the coprecipitates is reduced in amplitude and broadened indicating that the acids are adsorbed to ferrihydrite via carboxyl ligand exchange between the OH of the carboxyl group and the OH of an adsorption site[14]. It is also apparent, however, that, compared to their respective standards, the peak for these coprecipitates is shifted to lower energy and that this shift becomes increasingly pronounced with increasing number of carboxyl groups (Supplementary Table 2). The shift is remarkably consistent for the mono-, di- and tri-carboxyl coprecipitates over the range of molar OC (average shift from respective standards = −0.1 ± 0, −0.2 ± 0.04 and −0.4 ± 0 eV, respectively) and is therefore corroborated in data subsets with approximately equivalent molar OC and increasing n/constant m (e.g., Fh_Pen1/5_0.044 – Fh_Pen2/5_0.043 – Fh_Eth3/5_0.048 offset

Supplementary Fig. 3 and Supplementary Fig. 4 for extended discussion).

The theoretical adsorption capacities of the mono-, di- and majority of the tri-carboxyl coprecipitates provide between ~1 and 99% more sequestration capacity than would be required to accommodate all our OC in a monolayer at the particle surfaces (Supplementary Data 2). The theoretical adsorption capacities for

from respective standards $= -0.1 \pm 0.05$, -0.2 ± 0.05 and -0.4 ± 0.05 eV, respectively), while remaining constant in those with approximately equivalent and also varying molar OC and constant n/increasing m (Supplementary Table 2 and Supplementary Fig. 5). Our carboxyl peak shift is therefore independent of molar OC and rather is a function of the number of carboxyl groups in the adsorbing molecule.

A similar carboxyl band shift is observed in Fourier transform infra-red spectra of dissolved NOM coprecipitated with ferrihydrite compared to the unreacted NOM, which becomes increasingly pronounced for coprecipitates with lower molar OC[14]. The carboxylic character of the adsorbing NOM is assumed to be relatively invariant, and thus the shift of the carboxyl band to increasingly lower frequency is interpreted to reflect an increasing number of carboxyl ligand exchange bonds per adsorbing molecule with decreasing OC adsorbed[14]. We have an increasing number of carboxyl groups in our adsorbing OC, and a shift of the carboxyl peak to increasingly lower energy that is independent of OC adsorbed. Our shift is thus indicative of an increasing number of carboxyl ligand exchange bonds per adsorbing acid molecule with increasing number of carboxyl groups.

The NEXAFS spectra also exhibit a broad shoulder feature centred at ~287.3 eV (Fig. 3 and Supplementary Data 3) corresponding to aliphatic carbon (287.1–288.2 eV; Supplementary Table 1). Compared to their respective standards, the shoulder feature for all the coprecipitates is increased in amplitude but also generally becomes more pronounced in data subsets with constant n/increasing m (e.g. comparing Fh_Met1/1_0.033 vs. Fh_Pen1/5_0.044). The aliphatic transition state is specifically attributed to the $1s$-σ^*_{C-H}/3p state[43], to mixed $1s$-$\pi^*_{CH3,CH2}$/3p Rydberg-like excitations of CH groups[44], or to a number of broad bands associated with the $1s$-σ^*_{C-H} states on the higher energy side together with some mixture of unresolved $1s$-π^* transitions on the low energy side[42,43]. Rydberg-like excitations of CH groups can be dampened by Rydberg-valence mixing between the groups, and enhanced by a comparative lack of Rydberg-valence mixing that might occur when the groups are involved in adsorptive interactions[45]. A progressive prominence of the shoulder feature with increasing number of total carbon atoms is therefore indicative of an increasing number of CH adsorptive interactions per adsorbing acid molecule with increasing number of total carbon atoms.

The STXM elemental distribution maps show that carbon and iron are highly spatially correlated, with carbon apparently more concentrated at the particle edges ($R^2 = 0.881$–0.945, Supplementary Fig. 6). In these samples, the particles are of varying thickness, and the particle edges are likely to be thinner than the interiors. The STXM signal at the edge regions therefore reflects carbon mainly located at the particle surfaces while the signal over the central regions reflects carbon also incorporated throughout the bulk interior. A concentration of carbon at the edges, as opposed to a more uniform distribution over the entire particle, therefore confirms our theoretical adsorption capacity calculations that carbon is mainly adsorbed, without substantial incorporation into the interior (see 'Methods' for extended discussion of thickness-dependent detection bias). It should be noted, however, that carbon appears to be distributed at the particle surfaces in patches (Supplementary Fig. 6Ac, Bc). While this is consistent with our theoretical adsorption capacity calculations for carbon adsorbed in a monolayer equivalent, the spatial resolution of STXM is not sufficient to distinguish whether the patches are truly monolayer or multilayer[46]. Thus, although all adsorbed OC in these samples can be accommodated as a monolayer equivalent, some patches may form multilayer conglomerations[37,38]. A continuum between monolayer

equivalent and multilayer conglomerations is consistent with our theoretical adsorption capacity calculations for our tri-carboxylic coprecipitates with the highest sequestrations that require multilayering to achieve their OC loadings and observations of NOM with minerals in sediments[38].

Increasing number of carboxyl groups promotes stable carbon sequestration.

To quantify the stability of the acids with ferrihydrite against release and oxidation, we exposed our coprecipitates to solutions typically used to either desorb or oxidise OC sequestered with iron (oxyhydr)oxides (see 'Methods'). We chose coprecipitates (Supplementary Data 1) encompassing a range of molar OC (excluding tri-carboxylic coprecipitates with the highest sequestrations) and including several data subsets with approximately constant molar OC and either increasing n/constant m or constant n/increasing m (see 'Methods').

In all desorption and oxidation experiments, removal or destruction of the OC is incomplete. The entire data set shows that, as the number of carboxyl groups increases, the percent OC remaining sequestered increases ($R^2 = 0.789$, Supplementary Fig. 7), with the tri-carboxyl coprecipitates retaining up to ~65, ~40 and ~32% OC after treatment with artificial seawater, sodium hydroxide and sodium hypochlorite, respectively (Fig. 4 and Supplementary Data 4). Additionally, the percent OC remaining is highest for artificial seawater, which is the least aggressive treatment towards OC release (see 'Methods'). (The coprecipitates were washed with ultrapure water immediately after synthesis, and so essentially all OC remains after further ultrapure water washes, Supplementary Fig. 8). All data subsets with increasing n/constant m corroborate the above trends (e.g. Fh_Pen1/5_0.044 – Fh_Pen2/5_0.043 – Fh_Eth3/5_0.048, $R^2 = 0.989$ with sodium hydroxide, Supplementary Fig. 7). Unlike the sequestration data, however, neither the entire data set ($R^2 = 0.264$, Supplementary Fig. 9) nor most of the data subsets with constant n/increasing m show a strong dependence on the number of total carbon atoms (e.g. Fh_Met1/1_0.055 up to Fh_Pen1/5_0.044 at final coprecipitate C:Fe ≈ 0.05, $R^2 = 0.120$ with sodium hydroxide, Supplementary Fig. 9). This suggests that the adsorptive interactions involving the CH groups identified with NEXAFS are relatively weak[37], so while they enhance affinity, they offer little resistance to desorption and oxidation. Thus, even for mono-carboxylic acids, a fraction of the OC is very strongly sequestered, and with increasing number of carboxyl groups, the acids are increasingly resistant to desorption and oxidation.

The increase in the percent OC remaining as a function of the number of carboxyl groups is moderated by the molar OC sequestered. The entire data set shows that as the molar OC sequestered increases the percent OC remaining decreases ($R^2 = 0.867$ with sodium hydroxide; Supplementary Fig. 10). All data subsets corroborate the above trend, with the percent OC remaining decreasing with increasing molar OC for all those with increasing n/constant m (e.g. Fh_Pen2/5_0.043 – FhEth3/5_0.048 = ~26/40% OC remaining vs. Fh_Pen2/5_0.756 – FhEth3/5_0.787 = ~11/17% OC remaining with sodium hydroxide) and constant n/increasing m (i.e. Fh_Pen2/5_0.043 vs. Fh_Pen2/5_0.756 = ~26 vs. ~11% OC remaining with sodium hydroxide). This suggests that, although the acids are adsorbed via a common carboxyl ligand exchange adsorption mechanism as a function of the number of carboxyl groups, binding strength heterogeneities in their local adsorption environment, caused by electrostatic repulsion and/or steric hindrance between more closely packed molecules and/or accumulation of molecules in multilayer conglomerations that extend away from the mineral surface[37,38], render molecules adsorbed at high C:Fe less strongly bound and thus more susceptible to desorption and oxidation[24]. The scatter within the entire data set is highest, and thus the relationship between molar
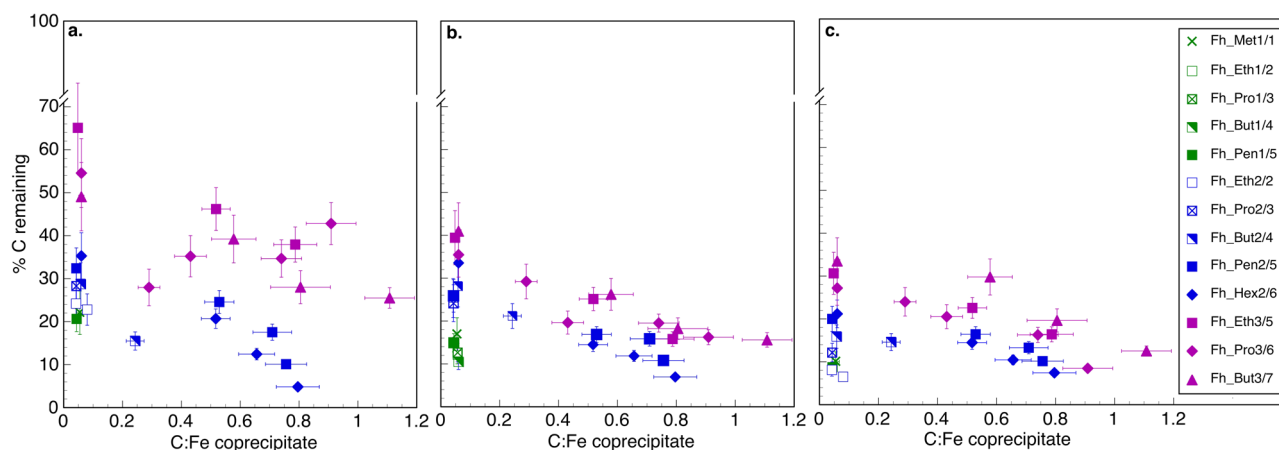
Fig. 4 Desorption and chemical stability of mono-, di- and tri-carboxylic acids coprecipitated with iron (oxyhydr)oxide ferrihydrite. Desorption and chemical oxidation data for carboxylic acid ferrihydrite coprecipitates plotted as C:Fe molar ratio coprecipitate vs. percent C remaining after treatment: **a** exposure to artificial seawater, **b** exposure to 0.1 M NaOH, and **c** oxidation with 1 M NaOCl. Green, blue and purple colour codes depict mono-, di- and tri-carboxylic data, respectively. The coprecipitate nomenclature is given in Fig. 1. Symbols are as follows: cross: Fh_Met1/1; open square: Fh_Eth1/2 and Fh_Eth2/2; crossed open square: Fh_Pro1/3 and Fh_Pro2/3; half solid square: Fh_But1/4 and Fh_But2/4; solid square: Fh_Pen1/5, Fh_Pen2/5 and Fh_Eth3/5; solid diamond: Fh_Hex2/6 and Fh_Pro3/6; solid triangle: Fh_But3/7. Data points and error bars represent the mean and one standard error of the mean (1 SEM) for triplicate coprecipitates each measured in triplicate (X axis), and the mean and one standard error of the mean (1 SEM) for triplicate coprecipitates each desorbed or chemically oxidised in triplicate and measured in triplicate (Y axis). Errors are propagated through all calculations using standard error propagation rules.

OC sequestered and percent OC remaining is weakest, for artificial seawater ($R^2 = 0.583$, Supplementary Fig. 10a). This suggests that binding strength heterogeneities are more pronounced during desorption with the least aggressive treatment.

Increasing number of carboxyl groups promotes persistent carbon sequestration. To quantify the persistence of the acids with ferrihydrite, we exposed our coprecipitates to sodium hydroxide and modelled desorption over time (see Methods). We chose only specific data subsets with approximately constant molar OC and increasing n/constant m, and increasing molar OC with constant n/constant m (see 'Methods').

All data subsets corroborate the stability experiments, where as the number of carboxyl groups or molar OC increases, the percent OC remaining increases or decreases, respectively. The subsets also show however, that the percent OC remaining decreases with time, in an apparently two-step desorption process, with up to ~70% of the OC removed within 1 h, followed by up to ~97% within 96 h (Fig. 5). The trends in the experimental data may be described using a two- or three-pool first-order kinetic model[47]. The two-pool model assumes one pool of desorbable carbon and a pool of non-desorbable carbon, while the three-pool model assumes two pools of desorbable carbon and a pool of non-desorbable carbon. In both models, the non-desorbable pool approaches an asymptote representing a fraction of OC that remains sequestered over the experimental timescale, similar to the G-model approach used to represent OC persistence in soils and sediments[47–49] (see 'Methods' for extended model descriptions and goodness-of-fit evaluation). The two-pool model provides adequate fits to the data but the non-desorbable pool is overestimated ($R^2 \geq 0.960$; model selection criteria average 2.85 ± 0.66; Supplementary Data 5 and Supplementary Fig. 11). This is likely because a two-pool model does not allow for sufficient binding strength heterogeneity in the local adsorption environment and thus in the apparent desorption rate of the desorbable pool[47]. The three-pool model provides better fits to the data by allowing for a slower desorption rate of one of the desorbable pools ($R^2 \geq 0.999$; model selection criteria average 6.06 ± 1.03; Supplementary Data 5 and Supplementary Fig. 11).
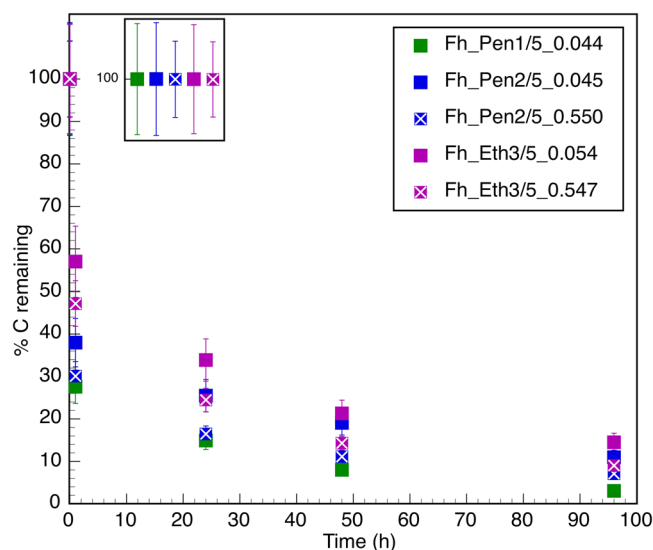

Fig. 5 Time series desorption of mono-, di- and tri-carboxylic acids coprecipitated with iron (oxyhydr)oxide ferrihydrite. Time series desorption data for carboxylic acid ferrihydrite coprecipitates plotted as time (h) vs. percent C remaining after exposure to 0.1 M NaOH. Green, blue and purple colour codes depict mono-, di- and tri-carboxylic data, respectively. The coprecipitate nomenclature is given in Fig. 1. Symbols are as follows: solid square: Fh_Pen1/5, Fh_Pen2/5 and Fh_Eth3/5 at ~0.05 C:Fe; crossed solid square: Fh_Pen2/5 and Fh_Eth3/5 at ~0.5 C:Fe. Data points and error bars represent the mean and one standard error of the mean (1 SEM) for duplicate coprecipitates each desorbed in duplicate and measured in duplicate. Errors are propagated through all calculations using standard error propagation rules.

Thus, over our experimental timescale, even for mono-carboxylic acids, a small fraction of OC persists with ferrihydrite (~2% for Fh_Pen1/5_0.044), and this fraction increases with an increasing number of carboxyl groups (up to ~11% for Fh_Eth3/5_0.054; ~8% for Fh_Eth3/5_0.547).

Discussion

The importance of OC coprecipitation and adsorption processes for regulating the global carbon cycle has been discussed for several decades[2,6,7,50]. A direct relationship between particular sequestration mechanisms and sequestration, stabilisation and persistence has not been established for coprecipitation or adsorption processes, however[30], and the controls on OC preservation remain poorly understood[51]. We investigate the role of carboxyl groups in the sequestration, stabilisation and persistence of OC during its coprecipitation with ferrihydrite. We show that simple carboxylic acids as model organic compounds are sequestered via an adsorption mechanism, in which carboxyl functional groups undergo ligand exchange with mineral hydroxyls. We show that an increasing number of carboxyl groups per acid molecule increases the number of carboxyl ligand exchange bonds formed between each molecule and the ferrihydrite particles. We conclude that this multi-carboxyl adsorption mechanism controls the enhanced sequestration, stability and persistence observed in our experiments. By extension, we propose that carboxyl-richness plays an important role in the sequestration, stability and persistence of more complex but typically carboxyl-rich NOM[34] during coprecipitation with and adsorption to iron (oxyhydr)oxides in soils and sediments.

In our coprecipitation experiments, we attribute the relationship between carboxyl-richness (increasing n/constant m), affinity, stability and persistence to a multi-carboxyl adsorption mechanism. The spectroscopic adsorption configuration of carboxylic acids with iron (oxyhydr)oxides is described in only a few studies, however, and the results are contradictory[52]; moreover, none evaluate the relationship between carboxyl-richness, stability and persistence. Adsorption of our mono-, di- and tri-carboxylic acids via an increasing number of carboxyl ligand exchange bonds per acid molecule is consistent with previous work in which mono-, di- and tri-carboxylic acids adsorb via one[53], two[54] or three[55] of their carboxyl groups, respectively (Supplementary Fig. 2). Di-carboxylic But2/4 (succinic) and Hex2/6 (adipic), however, may adsorb via just one of their carboxyl groups, possibly due to steric constraint on formation of a bidentate mononuclear structure[54], while tri-carboxylic Pro3/6 might adsorb via two carboxyl groups, although the exact adsorption configuration is unknown[56]. Both mono- and polycarboxylic acids may also form outer-sphere complexes (particularly at basic pH)[57,58]. Since our $\pi^*_{C=O}$ carboxyl carbon peak shift is constant for the mono- (-0.1 ± 0.0 eV), di- (-0.2 ± 0.04 eV) and tri-carboxylic acids (-0.4 ± 0.0 eV) (Fig. 3 and Supplementary Table 2), our results do not suggest substantial variation in the configuration of our molecules within each acid grouping, although we cannot rule out differences in configurations that result in unresolvable changes to the peak position.

In our coprecipitation experiments, we also observe a secondary affinity related to the number of total carbon atoms (constant n/increasing m), which enhances sequestration but does not significantly enhance stability or persistence. Enhanced sequestration of carboxylic acids with more acidic ($pK_a < 3$) carboxyl groups occurs during their adsorption on metal oxides[59]. Our acids however, have similar acidity (pK_{a1}, pK_{a2} and pK_{a3} all >3, except Eth2/2 and Pro2/3 $pK_{a1} < 3$) and do not become more acidic with increasing number of total carbon atoms (Fig. 1). Instead we attribute this secondary affinity to an increasing number of total carbon atoms and thus an increasing number of CH interactions per acid molecule occurring between the molecules and the ferrihydrite particles. These can involve either hydrogen bonding between CH groups and FeOH adsorption sites[60] and/or hydrophobic interactions between the CH groups of multiple OC moieties[37,61]. A reduction in our 1s-σ*$_{C-H}$/3p/1s-

π*$_{CH3,CH2}$/3p aliphatic carbon peak amplitudes for the mono-, di- and tri-carboxylic acids (Fig. 3) is consistent with increasing CH adsorptive interactions within each acid grouping. These interactions can also result in aliphatic hydrocarbons[62], polycarboxylic NOM analogues[25] and NOM[19] aligning parallel with iron (oxyhydr)oxide surfaces during adsorption, thus favouring formation of an increasing number of carboxyl ligand exchange bonds between the surfaces and increasingly carboxyl-rich molecules. Compared to carboxyl ligand exchange, however, CH interactions are relatively weak[37], so while they enhance sequestration, they do not enhance stability or persistence.

While we focus on an experimental coprecipitation system using simple carboxylic acids, by studying this system we determine a direct relationship between carboxyl-richness and sequestration, stability and persistence that we propose extends to NOM sequestration during coprecipitation processes with iron (oxyhydr)oxides in soils and sediments. At first glance, our experiments might not capture the breadth of coprecipitation processes occurring in natural environments. We use simple OC with few carboxyl groups and generate organominerals with relatively low C:Fe (<3 with those <1 subject to STXM NEXAFS and wet chemical treatments) in which OC is sequestered via a multi-carboxyl ligand exchange adsorption mechanism and predominantly located at particle surfaces in a monolayer equivalent. By comparison, NOM is extremely complex[28], with many carboxyl groups[34], and previous work indicates that hydroxyl groups, particularly those associated with carbon rings and in vicinal configuration, also play an important role in NOM sequestration[26]. As a likely consequence, experimental coprecipitation of NOM with iron (oxyhydr)oxides and also observations of NOM–iron (oxyhydr)oxide associations in the environment report equivalent[11] or often higher C:Fe, likely involving a combination of adsorption in monolayers and/or multilayers and incorporation into OC-Fe macromolecules and particle interiors[2,14,23,63]. In these studies, however, NOM sequestration is at least partly attributable to a carboxyl adsorption mechanism that tethers NOM to the mineral particles[14,63,64]. Moreover, carboxyl adsorption is suggested as the initially dominant process during organomineral microaggregate formation, rather than incorporation of OC into intraparticle pore spaces[63]. Furthermore, our theoretical adsorption capacity calculations and STXM NEXAFS indicate that, as we increase C:Fe in our tri-carboxylic coprecipitates, some multilayers of OC form, but these are still tethered to the particles via our multi-carboxyl adsorption mechanism. Thus, while multilayer interactions may enhance sequestration[14] and/or OC may become incorporated into macromolecules and particle interiors[23,63], we suggest that our multi-carboxyl adsorption mechanism plays a fundamental role in instigating OC uptake during natural coprecipitation processes.

Our results might also be extended to NOM sequestration during adsorption to preformed iron (oxyhydr)oxides in soils and sediments. At relatively low C:Fe (<1), the sequestration mechanism and spatial distribution of OC in our coprecipitation experiments and those with NOM[11] mirrors that seen in true adsorption experiments, where organics are also sequestered predominantly via a carboxyl adsorption mechanism at particle surfaces[14,25,26,65]. In these studies, O-rich groups, and in particular carboxyl groups attached to aromatic rings, are recently shown to be the first groups to adsorb to iron (oxyhydr)oxides and form a tether for subsequent multilayer interactions[66]. On the other hand, coprecipitation and adsorption processes might result in different chemical distributions of particular organic fractions between mineral and solution. Work on the chemical fractionation of NOM with iron (oxyhydr)oxides during coprecipitation and adsorption is limited and the results are contradictory, although fractionation may depend on NOM chemical

composition[14]. Using carboxyl-rich NOM, preferential sequestration of the carboxyl-rich component via carboxyl adsorption leads to an enrichment of the carboxyl fraction with the mineral, and the coprecipitated and adsorbed NOM have very similar chemical composition[14]. Using carboxyl-poor polysaccharide-rich NOM, preferential sequestration of the polysaccharide component occurs with a greater degree of enrichment during adsorption, and a non-uniform fractionation of individual sugar monomers occurs during the two sequestration processes[12]. Despite the differential sequestration of monosaccharides, however, the dominant sequestration mechanism is the same during coprecipitation and adsorption and predominantly involves carboxyl adsorption[12]. Given that these studies investigating adsorption[25,26,65,66] or both coprecipitation and adsorption[12,14] using a variety of different types of NOM all observe the predominance of a carboxyl adsorption mechanism, we suggest that our multi-carboxyl adsorption mechanism provides a mechanistic basis for understanding the chemical fractionation of NOM in the environment. Overall, although it is unlikely that all NOM carboxyl groups interact with iron (oxyhydr)oxide particles[18,19], their ubiquity in NOM and dominant involvement in NOM sequestration during both coprecipitation and adsorption processes strongly suggests that carboxyl-richness exerts an important control on NOM sequestration and chemical fractionation with these minerals in soils and sediments.

In soil environments, a carboxyl control on NOM preservation may contribute to observations that the relative proportion of carboxyl-rich NOM increases in mineral aggregates and with soil depth, and thus in the aged soil fraction[63,67]. While this is related to the enrichment of the carboxylic fraction during oxidative degradation[68], it is also consistent with an enhanced sequestration, stability and persistence of carboxyl-rich NOM with iron (oxyhydr)oxides. Similarly, our results offer mechanistic insight into frequently reported but apparently contradictory observations, where some mineral soils are enriched in aliphatic[69,70] while others contain a predominance of aromatic carbon[71,72]. Our work indicates that NOM preservation in soils is not necessarily related to these fractions, because carboxyl groups can be associated with both these components; rather NOM preservation will at least partly depend on its carboxyl-richness and the association of the carboxyl-rich fraction with iron (oxyhydr)oxides.

In marine environments, our work offers mechanistic insight into the generation and persistence of OC-iron phases in typical continental margin sediments underlain by oxic bottom waters whose molar C:Fe ratios (4.0 ± 2.8) far exceed those expected for monolayer adsorption[2,15]. We show that similarly elevated C:Fe are unlikely to be achieved simply in the presence of more NOM but rather require the presence of more carboxyl-rich NOM. Increasing carboxyl-richness then likely results in a continuum of OC–iron associations, including multilayers ('blebs') of NOM tethered to iron (oxyhydr)oxide surfaces[38] and incorporation of NOM into macromolecules and iron (oxyhydr)oxide particles[2]. Our work might also offer new insight into the enigmatic carboxyl-rich alicyclic molecules (CRAM) component of the dissolved NOM seawater pool[73]. Recent work indicates that marine sediments might be sources of CRAM to both sediment porewaters and the overlying water column[74], but the mechanism(s) that generate the CRAM signal are unknown[73]. Given the chemical fractionation of NOM with iron (oxyhydr)oxides towards carboxyl-rich components[14,66] and new work showing that OC–Fe colloidal organominerals diffuse out of marine sediments[75], we suggest that nanoscale OC–Fe colloids, macromolecules and nanoparticles carry a CRAM signal from the sediments into the overlying water column that might be measured as part of the dissolved NOM seawater pool.

Overall our work indicates that NOM sequestration, stability and persistence with iron (oxyhydr)oxides is strongly linked to its carboxyl-richness. A direct extrapolation of our work using iron (oxyhydr)oxides and carboxyl-richness alone to predict NOM persistence, however, is too simplistic. On the one hand, although a substantial proportion of OC is bound to iron (oxyhydr)oxides[2,15] and survives in these OC–iron phases for hundreds to thousands of years[2,9], clay minerals are also important for OC stabilisation against remineralisation[27]. Additionally, although NOM is carboxyl-rich[34] and associates with iron (oxyhydr)oxides predominantly via carboxyl adsorption[9,14], NOM is complex[28] and contains a variety of other groups that are also known to interact strongly with these minerals[26]. Instead our results provide a mechanistic framework that can be built upon to predict the affinity, stability and persistence of NOM in soils and sediments. We propose that in future work the link between other mineral sequestration mechanisms and OC persistence is similarly systematically investigated, so that a quantitative relationship between functional group-richness in simple OC moieties can be determined and then extended to more complex NOM. Together with improved understanding of the molecular composition of NOM[34], a combined molecular level and mechanistic approach might allow us to develop an overarching relationship between organic functional group-richness, mineral interactions and NOM preservation that is required to better understand the controls on the global carbon cycle.

Methods

Ferrihydrite and ferrihydrite carboxylic acid coprecipitate synthesis. Ferrihydrite was synthesised via the rapid hydrolysis of 0.1 M $Fe(NO_3)_3.9H_2O$ with 1 M KOH at pH ~7, under vigorous stirring at room temperature[76]. Carboxylic acid ferrihydrite coprecipitates were synthesised via the rapid hydrolysis of ferrihydrite as above but in the presence of different mono-, di- and tri-carboxylic acids (Fig. 1). Each coprecipitate was synthesised in triplicate and up to 11 different coprecipitate triplicates were generated for each carboxylic acid by sequentially increasing the concentration of C used in the rapid hydrolysis, while keeping the concentration of Fe constant. The initial solution C:Fe molar ratios for most coprecipitates ranged from 0.005 to 10.100, depending on the solubility limit of the carboxylic acid (Supplementary Data 1). Ferrihydrite and coprecipitates were gravitationally separated from the synthesis solution and then washed multiple times with ultrapure water (18.2 MΩ.cm) over a period of 4–5 days until the wash solution was between pH 5 and 7. Ferrihydrite and coprecipitates were stored as wet slurries at 4 °C.

Elemental analysis. Total C contents of the ferrihydrite and coprecipitate triplicates were determined on freeze-dried subsamples using a LECO SC-144DR Dual Range Sulphur and Carbon Analyser. Standard medium C and low C soil (no. 502-309, lot no. 1012) were used as analytical standards. Total C content of ferrihydrite was subtracted from total C contents of the coprecipitates to obtain final coprecipitate C contents. Total Fe content of the ferrihydrite and coprecipitate triplicates was determined by inductively coupled plasma mass spectrometry. For complete digestion, 1 mL of 1 M HCl was added to 0.2 mg sample in 10 mL glass vials and then subsequently diluted 10-fold with ultrapure water to obtain 1% (v/v) HCl. All elemental analyses were performed in triplicate.

Surface area analysis. The specific surface area of the ferrihydrite and selected coprecipitate triplicates was determined on freeze-dried subsamples by the multipoint Brunauer–Emmett–Teller method using a Micromeritics Gemini VII 2390a Surface Area Analyser. Samples were degassed at room temperature for 24 h using N_2 (g) (<1 ppm CO_2 (g)) prior to analysis. Graphite was used as an analytical standard. All specific surface area analyses were performed in triplicate.

X-ray diffraction. Mineralogy of the ferrihydrite and selected coprecipitate triplicates was confirmed on freeze-dried subsamples using a Bruker D8 Diffractometer with Cu-Kα radiation (λ ≈ 0.154 nm). Diffractograms were recorded from 2–90° 2θ with 0.02° 2θ step size and 930 ms acquisition time. Silicon dioxide was used as an analytical standard. Coprecipitate triplicates were homogenised into a single subsample prior to analysis.

STXM/NEXAFS spectroscopy. Coprecipitate triplicates were selected directly from the coprecipitation experiments covering a range of molar OC (from Fh_Met1/1_0.033 to Fh_But3/7_1.943) excluding the tri-carboxylic coprecipitates

at their highest surface coverages (i.e. those that exceeded estimated monolayer coverage) and including several data subsets each with approximately constant molar OC and either increasing n/constant m (increasing number of carboxyl groups and constant number of total carbon atoms: Fh_Pen1/5_0.044 *vs*. Fh_Pen2/5_0.043 vs. Fh_Eth3/5_0.048; and Fh_Hex2/6_0.796 vs. Fh_Pro3/6_0.909) or constant n/increasing m (constant number of carboxyl groups and increasing number of total carbon atoms: Fh_Met1/1_0.033 vs. Fh_Pen1/5_0.044; up to Fh_Pro3/6_0.909 vs. Fh_But3/7_1.108). Three coprecipitate triplicates were analysed over a range of molar OC (Fh_Pen2/5_0.043/0.709; Fh_Pro3/6_0.290/0.909; and Fh_But3/7_1.108/1.943). C 1s STXM NEXAFS spectra of the selected coprecipitates were recorded on Beamline I08, Diamond Light Source Ltd, Oxfordshire, UK. Coprecipitate triplicates were homogenised into a single subsample prior to analysis by resuspending ~2 mg of each coprecipitate triplicate in ~500 µL of ultrapure water and sonicating. An aliquot of ~5 µL of suspension was then pipetted onto a Si_3N_4 membrane window (Silson Ltd) and left to air dry. The membrane windows were glow discharged prior to loading with sample to improve particle distribution. Windows were then inserted into a high vacuum environment ($<1 \times 10^{-5}$ mBar) and analysed in scanning transmission mode. Stack data sets for C were collected from 275 to 310 eV, using varied energy resolution across different spectral regions of 0.5, 0.1 and 0.2 eV step size for pre-edge, running up to and over the edge, and post-edge, respectively. To maximise spectral resolution, the beamline uses Fresnel zone plates to focus the beam and a collimated plane grating monochromator of SX700-type with an undulator that provides a source size of 300 µm in the horizontal and 50 µm in the vertical plane, which was then refocussed into a secondary source with a 50 µm slit, providing an absolute energy resolution of better than 0.05 eV at the C K-edge. To minimise beam damage on the sample, dwell times were set to 10 ms per energy step following beam damage tests conducted by repeatedly measuring the same area of sacrificial samples. Beam damage manifests as a C NEXAFS peak at an absolute energy of 285.2 eV, attributable to the formation of aromatic C in the beam[77]. Sacrificial spectra with beam damage were discarded but the position of the aromatic C peak was used for absolute energy calibration by shifting all spectra in energy space by the required energy to align the beam damage peak to 285.2 eV. Reference spectra for the unreacted acids were obtained from unmodified acid solids or liquids as applicable. The dark signal was measured routinely by scanning a small area with the sample shutter closed. X-ray absorption stacks were aligned using the Axis2000 software. Spectra were extracted from the edge regions of individual coprecipitate particles and the dark signal was subtracted from the raw data using the Mantis software. Spectra were then exported for baseline correction, alignment, calibration and normalisation using the Athena software[78]. Baseline correction and normalisation avoid spectral dependence on the total C content, and as such, spectral features and peak shifts are indicative of C molecular structure and chemistry and not carbon concentration effects occurring during NEXAFS measurement. Peak identification for the normalised spectra was achieved with reference to literature assignments (Supplementary Table 1).

To show the spatial correlation between C and Fe, C and Fe elemental distribution maps were first created by aligning and then converting C and Fe images to optical density (OD) by using the transmitted flux through the sample (I) and the incident flux measured in an empty region adjacent to the analysed particles ($I0$) where OD = $ln(I0/I)$. C and Fe distribution maps taken on the same region of interest and with the same number of pixels were then aligned to common reference features and overlapped. To determine the C-Fe correlation coefficients, elemental thickness values on a pixel-by-pixel basis were compared by extracting the OD values using the Axis 2000 software, saved as an ascii file, and then the OD values for both C and Fe stacks were plotted against one another. The energies for obtaining the C and Fe distribution maps were C 1s 282.0–289.0 eV and Fe 2p 705.0–712.0 eV. According to Lambert Beer's law, the OD is directly proportional to the amount (thickness) of the element of interest in the X-ray beam path. It should be noted that, because the lowest energy used for the mapping is for C, and because heavier elements (mainly Fe) in the particles will absorb X-rays, C is not quantitatively mapped for particles with varying thickness. Regions where the particles are relatively thin will appear to be more concentrated in C than regions where the particles are relatively thick. Relative changes in OD across a particle are therefore not necessarily indicative of C distribution. For particles of varying thickness, however, the edge regions are generally thinner than the central regions, and thus the STXM signal at the edge regions reflects C mainly located at the particle surfaces, while the STXM signal in the central regions reflects C located at the particle surfaces and in the particle interiors. If C appears to be more concentrated at the edge regions than the central regions, then the distribution of C across the whole particle is approximately equal to that at the particle surfaces and is not substantially augmented in the central regions by additional C associated with the greater particle volume. In this case then, C distribution can be interpreted to be mainly at the particle surfaces, without substantial sequestration into the particle interior.

Desorption and oxidation. Coprecipitate triplicates were selected directly from the coprecipitation experiments covering a range of molar OC (from Fh_Met1/1_0.055 to Fh_But3/7_1.108) excluding the tri-carboxylic coprecipitates at their highest surface coverages (i.e. those that exceeded estimated monolayer coverage) and including several data subsets each with approximately constant molar OC and

either increasing n/constant m (increasing number of carboxyl groups and constant number of total carbon atoms) or constant n/increasing m (constant number of carboxyl groups and increasing number of total carbon atoms). Desorption of OC from the selected coprecipitate triplicates was achieved using artificial seawater (pH 8) and 0.1 M NaOH (pH 12), while chemical stability of OC associated with the selected coprecipitate triplicates was tested via oxidation with NaOCl[24,79]. Use of NaOCl affects Fe (oxyhydr)oxides less strongly than H_2O_2*[24,79]. Wet coprecipitate slurry was mixed with either artificial seawater or 0.1 M NaOH at a solid:solution ratio of 5 g dry coprecipitate L^{-1}, and samples were gently agitated end-over-end for 24 h. Solids were separated by centrifugation and the dilution cycle was repeated for a total of five cycles. After the last cycle, solids were separated and freeze-dried for elemental analysis. All elemental analyses were performed in triplicate. Wet coprecipitate slurry was mixed with 1 M NaOCl at a solid:solution ratio of 10 g dry coprecipitate L^{-1}, and samples were gently agitated end-over-end at room temperature for 6 h. Carboxylic acids exhibit a reverse adsorption edge on iron (oxyhydr)oxide particles with desorption beginning >pH 3.5[26]. The pH of the 1 M NaOCl was therefore set to pH 3.5 using a few µL of concentrated HCl to ensure that OC removal was due to reduction-release only. After the designated reaction time, solids were separated and freeze-dried for elemental analysis. All elemental analyses were performed in triplicate. Given the reverse adsorption edge for carboxylic acids on iron (oxyhydr)oxides[26], the artificial seawater treatment at pH 8 is the least aggressive towards OC release, while the 0.1 M NaOH at pH 12 and the 1 M NaOCl, which chemically oxidises OC, are the most aggressive towards OC release. It should be noted that the selected coprecipitate triplicates were also washed with ultrapure water set at pH 3.5 as described above for artificial seawater and 0.1 M NaOH, although because the samples were washed with ultrapure water immediately after their synthesis this wash was not expected to result in significant desorption.

Desorption of OC from selected coprecipitate duplicates reproduced from the coprecipitation experiments was also performed with 0.1 M NaOH as a function of time in a batch desorption approach, with coprecipitate duplicates chosen and individual experiments set up as above for the first desorption cycle but sacrificed at 1, 24, 48 and 96 h (data subset with approximately constant molar OC and increasing n/constant m Fh_Pen1/5_0.044 vs. Fh_Pen2/5_0.045 vs. Fh_Eth3/5_0.054; and data subsets with increasing molar OC with constant n/constant m Fh_Pen2/5_0.045 vs. Fh_Pen2/5_0.550 and Fh_Eth3/5_0.054 vs. Fh_Eth3/5_0.547). After the designated desorption time, solids were separated and freeze-dried for elemental analysis. All elemental analyses were performed in duplicate. In all desorption and oxidation experiments, total OC desorbed or released was calculated as the difference between the initial C content of each coprecipitate and the final C content after desorption or oxidation.

Theoretical adsorption capacity. To define the theoretical adsorption capacity, we considered the surface coverage of a monolayer, in which either just one COOH group from each acid molecule binds to a FeOH adsorption site (referred to here as one-carboxyl adsorption and resulting in the maximum monolayer OC loading for the number of adsorption sites) or all COOH groups from each acid molecule each bind to a FeOH adsorption site (resulting in two- and three-carboxyl adsorption for di- and tri-carboxylic acids, respectively, and the minimum monolayer OC loading for the number of adsorption sites). We neglected any steric or electrostatic hindrance resulting from the close packing of the acid molecules in the one-, two- and three-carboxyl scenarios and assumed that carboxyl binding can occur using every FeOH adsorption site. Spectroscopic evidence indicates that, in a one-carboxyl scenario, the mono-, di- and tri-carboxylic acids could adsorb using only one carboxyl group per adsorbing acid molecule, and this carboxyl group binds to one FeOH adsorption site, in either a single-bonded or twice-bonded configuration[53,54] (Supplementary Fig. 3a). In theory, the one-carboxyl twice-bonded configuration is the 'worst case scenario' for one-carboxyl adsorption because, compared to the single-bonded configuration, it tethers one carboxyl group to the surface but requires two FeOH adsorption sites, while the single-bonded configuration similarly tethers one carboxyl group but requires only one FeOH adsorption site. Spectroscopic evidence indicates that, in a two-carboxyl scenario, the di- and tricarboxylic acids could adsorb using two carboxyl groups per adsorbing acid molecule, and these carboxyl groups bind to either one FeOH site (bidentate mononuclear) or two FeOH sites (bidentate binuclear)[54] (Supplementary Fig. 3b). In theory, the bidentate binuclear configuration provides the 'worst case scenario' for two-carboxyl adsorption because, compared to the bidentate mononuclear configuration, it tethers two carboxyl groups to the particle surface but requires two FeOH sites, while the bidentate mononuclear configuration similarly tethers two carboxyl groups to the particle surface but requires only one FeOH site. Spectroscopic evidence indicates that, in a three-carboxyl scenario, the tri-carboxylic acids could adsorb using three carboxyl groups per adsorbing acid molecule, and these carboxyl groups bind to three FeOH sites (tridentate trinuclear)[55] (Supplementary Fig. 3c). To calculate the theoretical adsorption capacity, we then used the fact that there are 5.8 FeOH adsorption sites nm^{-2} as recently determined from an analysis of the ferrihydrite surface structure[80]. It should be noted that, in the one-carboxyl single-bonded scenario (where the acids adsorb via one carboxyl group per adsorbing acid molecule to one FeOH site), with 5.8 sites nm^{-2} and 1 COOH group/site, each COOH group occupies ~0.17 nm^2, which is comparable to 0.205 nm^2 estimated for the adsorption of a COOH group to hydrous γAl_2O_3*[59].

To calculate the measured surface adsorption (mg C m^{-2}), we nominally assumed that all our measured OC (mg C g^{-1}) is adsorbed in a monolayer at the particle surfaces (m^2 g^{-1}). The specific surface area for the pure ferrihydrite and the ferrihydrite coprecipitates are 333 ± 14.8 m^2 g^{-1} and between ~327 ± 17.0 and 202 ± 9.1 m^2 g^{-1}, respectively (Supplementary Data 1), and show that, in the presence of the carboxylic acids, ferrihydrite appears to possess a significantly lower specific surface area and thus a larger particle size. X-ray diffraction of the coprecipitates, however, shows that, as the number of carboxyl groups increases, the crystallinity of the ferrihydrite decreases (Supplementary Fig. 4). This counterintuitive effect is likely because the ferrihydrite surface is somewhat masked by the adsorbed carboxylic acid, and OC molecules have a comparatively much lower specific surface area[11,81]. In keeping with previous work on the sorption of OC to iron (oxyhydr)oxides[11] we therefore assumed that the ferrihydrite fraction of the coprecipitates has at least the same specific surface area as the pure ferrihydrite, i.e. 333 m^2 g^{-1}.

In the main text, the theoretical adsorption capacities of the coprecipitates for the 'worst case scenarios' for one-, two- and three-carboxyl adsorption (i.e. one-carboxyl twice-bonded, bidentate binuclear and tridentate trinuclear configurations, respectively) are compared to the OC loading.

Kinetic desorption experiment modelling. The kinetics of desorption can be described as a first-order expression as follows[82]:

$$\frac{d\theta}{dt} = -k\theta \tag{1}$$

where θ is the concentration of sorbate, t is time (h) and k is the apparent desorption constant (h^{-1}). Considering two pools of OC, one for desorbable carbon and one for non-desorbable carbon, the above equation can be solved as[47]:

$$\theta_t = \theta_0 e^{-kt} + \theta_\infty \tag{2}$$

where θ_t is the total concentration of carbon associated with the ferrihydrite particles, θ_0 is the concentration of desorbable carbon at time zero, θ_∞ is the concentration of non-desorbable carbon where the modelled carbon approaches an asymptote and, as above, k is the apparent desorption rate (h^{-1}) and t is time (h). Similar to the concept of the multi-G model[49,83] for the degradation of organic matter, a three-pool model may also be considered, with two pools of desorbable carbon and a pool of non-desorbable carbon as follows[47]:

$$\theta_t = \theta_{01} e^{-k_1 t} + \theta_{02} e^{-k_2 t} + \theta_\infty \tag{3}$$

where θ_t is the total concentration of carbon associated with the ferrihydrite particles, θ_{01} is the concentration of highly desorbable carbon at time zero, θ_{02} is the concentration of less desorbable carbon at time zero, θ_∞ is the concentration of non-desorbable carbon where the modelled carbon approaches an asymptote, k_1 and k_2 are the apparent desorption rates of the highly and less desorbable carbon (h^{-1}), respectively, and, as above, t is time (h).

To determine the preferred model, we calculated the R^2 and the model selection criteria, the latter of which allows comparison between models with a different number of fitting parameters and where a higher value signifies a better goodness of fit for a smaller number of parameters[84].

The two-pool model provides adequate fits to the data ($R^2 \geq 0.960$ in all cases; model selection criteria average over all cases 2.85 ± 0.66; Supplementary Data 5 and Supplementary Fig. 11). Commensurate with the stability experiments, the desorbable pool and apparent desorption rate decrease with increasing number of carboxyl groups and increase with increasing molar OC sequestered. The non-desorbable pool increases with increasing number of carboxyl groups and decreases with increasing molar OC sequestered, but it is overestimated in all cases. The three-pool model provides better fits to the data ($R^2 \geq 0.999$ in all cases; model selection criteria average over all cases 6.06 ± 1.03; Supplementary Data 5 and Supplementary Fig. 11) by allowing for a slower desorption rate of one of the desorbable pools. This results in a highly desorbable pool and apparent desorption rate that decrease with increasing number of carboxyl groups and increase with increasing molar OC sequestered but a less desorbable pool with a lower desorption rate that increases with increasing number of carboxyl groups and decreases with increasing molar OC sequestered. In agreement with the two-pool model, the non-desorbable pool increases with increasing number of carboxyl groups and decreases with increasing molar OC sequestered but without overestimation.

Data availability
All source data for the tables and figures presented in this manuscript and the Supplementary Information is available in the Supplementary Data files, which are also deposited to the general data repository Figshare and can be accessed at https://doi.org/10.6084/m9.figshare.16408317. The Supplementary Data files contain the source data for Figs. 2, 3, 4 and 5, and Supplementary Figs. 1, 2, 5, 7, 8, 9, 10 and 11.

References
1. Eglinton, T. I. A rusty carbon sink. *Nature* **483**, 165–166 (2012).
2. Lalonde, K., Mucci, A., Ouellet, A. & Gélinas, Y. Preservation of organic matter in sediments promoted by iron. *Nature* **483**, 198–200 (2012).
3. Schmidt, M. W. I. et al. Persistence of soil organic matter as an ecosystem property. *Nature* **478**, 49–56 (2011).
4. Lehmann, J. & Kleber, M. The contentious nature of soil organic matter. *Nature* **528**, 60–68 (2015).
5. Davidson, E. A. & Janssens, I. A. Temperature sensitivity of soil carbon decomposition and feedbacks to climate change. *Nature* **440**, 165–173 (2006).
6. Kramer, M. G. & Chadwick, O. A. Climate-driven thresholds in reactive mineral retention of soil carbon at the global scale. *Nat. Clim. Change* **8**, 1104–1108 (2018).
7. Hedges, J. I. & Keil, R. G. Sedimentary organic matter preservation: an assessment and speculative synthesis. *Mar. Chem.* **49**, 81–115 (1995).
8. Raiswell, R. & Canfield, D. E. The iron biogeochemical cycle past and present. *Geochem. Perspect.* **1**, 1–2 (2012).
9. Kaiser, K. & Guggenberger, G. The role of DOM sorption to mineral surfaces in the preservation of organic matter in soils. *Org. Geochem.* **31**, 711–725 (2000).
10. Sposito, G. *The Chemistry of Soils* (Oxford University Press, 2008).
11. Eusterhues, K. et al. Characterization of ferrihydrite-soil organic matter coprecipitates by X-ray diffraction and Mossbauer spectroscopy. *Environ. Sci. Technol.* **42**, 7891–7897 (2008).
12. Eusterhues, K. et al. Fractionation of organic matter due to reaction with ferrihydrite: coprecipitation versus adsorption. *Environ. Sci. Technol.* **45**, 527–533 (2011).
13. Mikutta, R., Lorenz, D., Guggenberger, G., Haumaier, L. & Freund, A. Properties and reactivity of Fe-organic matter associations formed by coprecipitation versus adsorption: clues from arsenate batch adsorption. *Geochim. Cosmochim. Acta* **144**, 258–276 (2014).
14. Chen, C., Dynes, J. J., Wang, J. & Sparks, D. L. Properties of Fe-organic matter associations via coprecipitation versus adsorption. *Environ. Sci. Technol.* **48**, 13751–13759 (2014).
15. Wagai, R. & Mayer, L. M. Sorptive stabilization of organic matter in soils by hydrous iron oxides. *Geochim. Cosmochim. Acta* **71**, 25–35 (2007).
16. ThomasArrigo, L. K., Mikutta, C., Byrne, J., Kappler, A. & Kretzschmar, R. Iron (II)-catalyzed iron atom exchange and mineralogical changes in iron-rich organic freshwater flocs: an iron isotope tracer study. *Environ. Sci. Technol.* **51**, 6897–6907 (2017).
17. Henneberry, Y. K., Kraus, T. E. C., Nico, P. S. & Horwath, W. R. Structural stability of coprecipitated natural organic matter and ferric iron under reducing conditions. *Org. Geochem.* **48**, 81–89 (2012).
18. Eusterhues, K. et al. Reduction of ferrihydrite with adsorbed and coprecipitated organic matter: microbial reduction by *Geobacter bremensis* vs. abiotic reduction by Na-dithionite. *Biogeosciences* **11**, 4953 (2014).
19. Chen, C., Kukkadapu, R. & Sparks, D. L. Influence of coprecipitated organic matter on Fe2+ (aq)-catalyzed transformation of ferrihydrite: implications for carbon dynamics. *Environ. Sci. Technol.* **49**, 10927–10936 (2015).
20. Schwertmann, U. Inhibitory effect of soil organic matter on the crystallization of amorphous ferric hydroxide. *Nature* **212**, 645–646 (1966).
21. ThomasArrigo, L. K., Byrne, J. M., Kappler, A. & Kretzschmar, R. Impact of organic matter on iron (II)-catalyzed mineral transformations in ferrihydrite–organic matter coprecipitates. *Environ. Sci. Technol.* **52**, 12316–12326 (2018).
22. Henrichs, S. M. Sedimentary organic matter preservation: an assessment and speculative synthesis—a comment. *Mar. Chem.* **49**, 127–136 (1995).
23. Lehmann, J. et al. Spatial complexity of soil organic matter forms at nanometre scales. *Nat. Geosci.* **1**, 238–242 (2008).
24. Kaiser, K. & Guggenberger, G. Sorptive stabilization of organic matter by microporous goethite: sorption into small pores vs. surface complexation. *Eur. J. Soil Sci.* **58**, 45–59 (2007).
25. Gu, B., Schmitt, J., Chen, Z., Liang, L. & McCarthy, J. F. Adsorption and desorption of natural organic matter on iron oxide: mechanisms and models. *Environ. Sci. Technol.* **28**, 38–46 (1994).
26. Gu, B., Schmitt, J., Chen, Z., Liang, L. & McCarthy, J. F. Adsorption and desorption of different organic matter fractions on iron oxide. *Geochim. Cosmochim. Acta* **59**, 219–229 (1995).
27. Mikutta, R. et al. Biodegradation of forest floor organic matter bound to minerals via different binding mechanisms. *Geochim. Cosmochim. Acta* **71**, 2569–2590 (2007).
28. Hertkorn, N. et al. Natural organic matter and the event horizon of mass spectrometry. *Anal. Chem.* **80**, 8908–8919 (2008).
29. Aufdenkampe, A. K., Hedges, J. I., Richey, J. E., Krusche, A. V. & Llerena, C. A. Sorptive fractionation of dissolved organic nitrogen and amino acids onto fine sediments within the Amazon Basin. *Limnol. Oceanogr.* **46**, 1921–1935 (2001).

30. Kleber, M. et al. Dynamic interactions at the mineral–organic matter interface. *Nat. Rev. Earth Environ.* **2**, 402–421 (2021).

31. Jones, D. L. Organic acids in the rhizosphere–a critical review. *Plant Soil* **205**, 25–44 (1998).

32. Barcelona, M. J. Dissolved organic carbon and volatile fatty acids in marine sediment pore waters. *Geochim.Cosmochim. Acta* **44**, 1977–1984 (1980).

33. Hemingway, J. D. et al. Mineral protection regulates long-term global preservation of natural organic carbon. *Nature* **570**, 228–231 (2019).

34. Zark, M. & Dittmar, T. Universal molecular structures in natural dissolved organic matter. *Nat. Commun.* **9**, 1–8 (2018).

35. Sparks, D. L. *Environmental Soil Chemistry* (Elsevier, 2003).

36. Mayer, L. M. Extent of coverage of mineral surfaces by organic matter in marine sediments. *Geochim. Cosmochim. Acta* **63**, 207–215 (1999).

37. Wershaw, R. L. *Membrane-micelle Model for Humus in Soils and Sediments and its Relation to Humification* (US Geological Survey, USGPO, 1994).

38. Ransom, B., Bennett, R., Baerwald, R. & Shea, K. TEM study of in situ organic matter on continental margins: occurrence and the "monolayer" hypothesis. *Mar. Geol.* **138**, 1–9 (1997).

39. Vogel, N., Retsch, M., Fustin, C.-A., del Campo, A. & Jonas, U. Advances in colloidal assembly: the design of structure and hierarchy in two and three dimensions. *Chem. Rev.* **115**, 6265–6311 (2015).

40. Eusterhues, K., Rumpel, C. & Kögel-Knabner, I. Organo-mineral associations in sandy acid forest soils: importance of specific surface area, iron oxides and micropores. *Eur. J. Soil Sci.* **56**, 753–763 (2005).

41. Johnson, K. et al. Towards a mechanistic understanding of carbon stabilization in manganese oxides. *Nat. Commun.* **6**, 1–11 (2015).

42. Solomon, D. et al. Carbon (1s) NEXAFS spectroscopy of biogeochemically relevant reference organic compounds. *Soil Sci. Soc. Am. J.* **73**, 1817–1830 (2009).

43. Kaznacheyev, K. et al. Innershell absorption spectroscopy of amino acids. *J. Phys. Chem. A* **106**, 3153–3168 (2002).

44. Hitchcock, A. P. & Ishii, I. Carbon K-shell excitation spectra of linear and branched alkanes. *J. Electron Spectrosc. Relat. Phen.* **42**, 11–26 (1987).

45. Otero, E. & Urquhart, S. G. Nitrogen 1s near-edge X-ray absorption fine structure spectroscopy of amino acids: resolving zwitterionic effects. *J. Phys. Chem. A* **110**, 12121–12128 (2006).

46. Possinger, A. R. et al. Organo–organic and organo–mineral interfaces in soil at the nanometer scale. *Nat. Commun.* **11**, 1–11 (2020).

47. Shields, M. R., Bianchi, T. S., Gélinas, Y., Allison, M. A. & Twilley, R. R. Enhanced terrestrial carbon preservation promoted by reactive iron in deltaic sediments. *Geophys. Res. Lett.* **43**, 1149–1157 (2016).

48. Berner, R. A. An idealized model of dissolved sulfate distribution in recent sediments. *Geochim. Cosmochim. Acta* **28**, 1497–1503 (1964).

49. Westrich, J. T. & Berner, R. A. The role of sedimentary organic matter in bacterial sulfate reduction: the G model tested. *Limnol. Oceanogr.* **29**, 236–249 (1984).

50. Keil, R. G., Montluçon, D. B., Prahl, F. G. & Hedges, J. I. Sorptive preservation of labile organic matter in marine sediments. *Nature* **370**, 549–552 (1994).

51. Arndt, S. et al. Quantifying the degradation of organic matter in marine sediments: a review and synthesis. *Earth Sci. Rev.* **123**, 53–86 (2013).

52. Han, J., Kim, M. & Ro, H.-M. Factors modifying the structural configuration of oxyanions and organic acids adsorbed on iron (hydr) oxides in soils. A review. *Environ. Chem. Lett.* **18**, 631–662 (2020).

53. Dobson, K. D. & McQuillan, A. J. In situ infrared spectroscopic analysis of the adsorption of aliphatic carboxylic acids to TiO_2, ZrO_2, Al_2O_3, and Ta_2O_5 from aqueous solutions. *Spectrochim. Acta A Mol. Biomol. Spectrosc.* **55**, 1395–1405 (1999).

54. Duckworth, O. W. & Martin, S. T. Surface complexation and dissolution of hematite by C1-C6 dicarboxylic acids at pH= 5.0. *Geochim. Cosmochim. Acta* **65**, 4289–4301 (2001).

55. Cornell, R. & Schindler, P. Infrared study of the adsorption of hydroxycarboxylic acids onα-FeOOH and amorphous Fe (III) hydroxide. *Colloid Polym. Sci.* **258**, 1171–1175 (1980).

56. Lindegren, M., Loring, J. S. & Persson, P. Molecular structures of citrate and tricarballylate adsorbed on α-FeOOH particles in aqueous suspensions. *Langmuir* **25**, 10639–10647 (2009).

57. Hwang, Y. S. & Lenhart, J. J. Adsorption of C4-dicarboxylic acids at the hematite/water interface. *Langmuir* **24**, 13934–13943 (2008).

58. Borowski, S. C. et al. Structure and reactivity of oxalate surface complexes on lepidocrocite derived from infrared spectroscopy, DFT-calculations, adsorption, dissolution and photochemical experiments. *Geochim. Cosmochim. Acta* **226**, 244–262 (2018).

59. Kummert, R. & Stumm, W. The surface complexation of organic acids on hydrous γ-Al2O3. *J. Colloid Interface Sci.* **75**, 373–385 (1980).

60. Hoffmann, R. W. & Brindley, G. W. Adsorption of non-ionic aliphatic molecules from aqueous solutions on montmorillonite. Clay-organic studies—II. *Geochim. Cosmochim. Acta* **20**, 15–29 (1960).

61. Evanko, C. R. & Dzombak, D. A. Surface complexation modeling of organic acid sorption to goethite. *J. Colloid Interface Sci.* **214**, 189–206 (1999).

62. Ta, T. D., Tieu, A. K., Zhu, H. & Kosasih, B. Adsorption of normal-alkanes on Fe (110), FeO (110), and Fe_2O_3 (0001): influence of iron oxide surfaces. *J. Phys. Chem. C* **119**, 12999–13010 (2015).

63. Lehmann, J., Kinyangi, J. & Solomon, D. Organic matter stabilization in soil microaggregates: implications from spatial heterogeneity of organic carbon contents and carbon forms. *Biogeochemistry* **85**, 45–57 (2007).

64. Solomon, D. et al. Micro-and nano-environments of carbon sequestration: multi-element STXM–NEXAFS spectromicroscopy assessment of microbial carbon and mineral associations. *Chem. Geol.* **329**, 53–73 (2012).

65. Lv, J. et al. Molecular-scale investigation with ESI-FT-ICR-MS on fractionation of dissolved organic matter induced by adsorption on iron oxyhydroxides. *Environ. Sci. Technol.* **50**, 2328–2336 (2016).

66. Coward, E. K., Ohno, T. & Sparks, D. L. Direct evidence for temporal molecular fractionation of dissolved organic matter at the iron oxyhydroxide interface. *Environ. Sci. Technol.* **53**, 642–650 (2018).

67. Fontaine, S. et al. Stability of organic carbon in deep soil layers controlled by fresh carbon supply. *Nature* **450**, 277–280 (2007).

68. Guggenberger, G., Kaiser, K. & Zech, W. Mobilization and immobilization of dissolved organic matter in forest soils. *Zeitschrift für Pflanzenernährung und Bodenkunde* **161**, 401–408 (1998).

69. Almendros, G., Guadalix, M. E., Gonzalez-Vila, F. J. & Martin, F. Preservation of aliphatic macromolecules in soil humins. *Org. Geochem.* **24**, 651–659 (1996).

70. Kögel-Knabner, I. et al. Organo-mineral associations in temperate soils: Integrating biology, mineralogy, and organic matter chemistry. *J. Plant Nutr. Soil Sci.* **171**, 61–82 (2008).

71. Avneri-Katz, S. et al. Adsorptive fractionation of dissolved organic matter (DOM) by mineral soil: macroscale approach and molecular insight. *Org. Geochem.* **103**, 113–124 (2017).

72. Kothawala, D. N., Roehm, C., Blodau, C. & Moore, T. R. Selective adsorption of dissolved organic matter to mineral soils. *Geoderma* **189**, 334–342 (2012).

73. Repeta, D. J. in *Biogeochemistry of Marine Dissolved Organic Matter* (eds Hansell, D. A. & Carlson, C. A.) Ch. 2 (Elsevier, 2015).

74. Fox, C. A., Abdulla, H. A., Burdige, D. J., Lewicki, J. P. & Komada, T. Composition of dissolved organic matter in pore waters of anoxic marine sediments analyzed by 1H nuclear magnetic resonance spectroscopy. *Front. Mar. Sci.* **5**, 172 (2018).

75. Homoky, W. B. et al. Iron colloids dominate sedimentary supply to the ocean interior. *Proc. Natl Acad. Sci.* **118**, e2016078118 (2021).

76. Schwertmann, U. & Cornell, R. *Iron Oxides in the Laboratory* (VCH Verlagsgesellschaft, 1991).

77. Zubavichus, Y., Shaporenko, A., Grunze, M. & Zharnikov, M. Innershell absorption spectroscopy of amino acids at all relevant absorption edges. *J. Phys. Chem. A* **109**, 6998–7000 (2005).

78. Ravel, B. & Newville, M. ATHENA, ARTEMIS, HEPHAESTUS: data analysis for X-ray absorption spectroscopy using IFEFFIT. *J. Synchr. Radiat.* **12**, 537–541 (2005).

79. Mikutta, R., Kleber, M., Kaiser, K. & Jahn, R. Organic matter removal from soils using hydrogen peroxide, sodium hypochlorite, and disodium peroxodisulfate. *Soil Sci. Soc. Am. J.* **69**, 120–135 (2005).

80. Hiemstra, T. & Zhao, W. Reactivity of ferrihydrite and ferritin in relation to surface structure, size, and nanoparticle formation studied for phosphate and arsenate. *Environ. Sci. Nano* **3**, 1265–1279 (2016).

81. Chiou, C. T., Lee, J. F. & Boyd, S. A. The surface area of soil organic matter. *Environ. Sci. Technol.* **24**, 1164–1166 (1990).

82. Lagergren, S. K. About the theory of so-called adsorption of soluble substances. *Sven. Vetenskapsakad. Handingarl* **24**, 1–39 (1898).

83. Jørgensen, B. B. A comparison of methods for the quantification of bacterial sulfate reduction in coastal marine sediments: I. Measurement with radiotracer techniques. *Geomicrobiol. J.* **1**, 11–27 (1978).

84. Saiers, J. E. & Hornberger, G. M. Migration of 137Cs through quartz sand: experimental results and modeling approaches. *J. Contam. Hydrol.* **22**, 255–270 (1996).

85. Kim, S. et al. PubChem in 2021: new data content and improved web interfaces. *Nucleic Acids Res.* **49**, D1388–D1395 (2021).

Acknowledgements

Author contributions

C.L.P formulated the original hypothesis. C.L.P., L.C. and O.W.M. designed the work reported here, interpreted the data and wrote the manuscript. P.B., K.-Q.X., C.W., A.W.B. and B.J.F. contributed to the work design and data interpretation. L.C. performed all the experiments and experimental analyses except B.J.F. collected the XRD data. C.L.P., L.C., O.W.M., M.K. and B.K. collected the synchrotron data and contributed to its processing and interpretation. All authors contributed to the preparation of the manuscript.

Competing interests

The authors declare no competing interests.

Additional information

Supplementary information The online version contains supplementary material available at https://doi.org/10.1038/s43247-021-00301-9.

Correspondence and requests for materials should be addressed to Caroline L. Peacock.

Peer review information *Communications Earth & Environment* thanks the anonymous reviewers for their contribution to the peer review of this work. Primary Handling Editor: Joshua Dean.

Reprints and permission information is available at http://www.nature.com/reprints

Publisher's note Springer Nature remains neutral with regard to jurisdictional claims in published maps and institutional affiliations.